Experiments in Fluids (2023) 64:53
https://doi.org/10.1007/s00348-023-03592-0

RESEARCH ARTICLE

Three-dimensional encoding of a gas–liquid interface by means of color-coded glare points

Maximilian Dreisbach[1] · Sebastian Blessing[1] · André Brunn[2] · Frank Michaux[2] · Alexander Stroh[1] · Jochen Kriegseis[1]

Received: 31 October 2022 / Revised: 24 January 2023 / Accepted: 28 January 2023

Abstract
The present work introduces an extension of the shadowgraphy method by differently colored oblique light sources for the observation of the three-dimensional spatio-temporal dynamics of gas–liquid interfaces. The proposed expanded approach is tested and elaborated with the example of a droplet during impingement. Particularly, it is elaborated in a combined experimental/theoretical approach, how well glare points from differently colored oblique light sources can be used to encode additional 3D information of the droplet shape within a single shadowgraph image. Narrow-banded LEDs with distinct spectra and maxima in the visible light illuminate the droplet from different angles in red, green and blue light, respectively, while a high-speed RGB camera captures the images produced by each light source in the corresponding image channel, therefore creating three unique views of the droplet. In order to compensate for the mutual perturbation of the images resulting from cross-talk between the channels and the polychromatic light of the LEDs, a color correction is introduced, which is based on the transfer function between the light sources and the channels of the RGB camera. In experiments with the proposed measurement setup of a water droplet impinging onto a flat substrate it is successfully demonstrated that three unique and independent grayscale images can be reconstructed with this color correction function. The optimal illumination angles for the lateral light sources are determined experimentally, which lead to consistent glare points on the deforming gas–liquid interface throughout the dynamic process of the drop impact. An ellipsoidal droplet is considered to derive information on orientation and three-dimensional shape of a non-axisymmetrical droplet from the relative positions of the glare points and the shadowgraph contour. Thereby it is successfully demonstrated that the additional three-dimensional information encoded in the glare points can lay the groundwork for the volumetric reconstruction of the deforming gas–liquid interface during the impingement of a droplet.

1 Introduction

The impact of liquid droplets onto both wet and dry surfaces is a key process for a wide range of technical applications. For example, in spray cooling, an optimization of the interaction between the droplet and the solid wall can lead to significant gains in efficiency (Ashgriz 2011). In spray coating, the prevention of air entrapment would improve the quality of the surface as outlined e.g., by Dalili et al. (2016). Various details of these processes, however, remain yet to be fully understood (Josserand and Thoroddsen 2016). Drop impact phenomena include splashing, receding, partial or complete rebound and deposition of the impinging droplet, and depend on the impact conditions—most importantly the velocity and size of the droplet and the angle of incidence, as well as the fluid properties and the roughness of the substrate (Yarin 2005).

The present work addresses the deposition type drop impact, as characterized by Rioboo et al. (2002). A commonly used optical measurement method for the observation of drop-impact dynamics is the shadowgraphy technique (Wakeham et al. 2007; Nitsche and Brunn 2006), wherein the falling droplet is illuminated in parallel backlight, mapping the contour of the droplet accurately and, therefore, allowing for a precise measurement of the gas–liquid interface. In combination with high-speed imaging this method can be used to measure the wetting properties and contact-line dynamics of drops impacting at different

✉ Maximilian Dreisbach
maximilian.dreisbach@kit.edu

[1] Institute of Fluid Mechanics (ISTM), Karlsruhe Institute of Technology (KIT), Kaiserstr. 10, 76131 Karlsruhe, Germany

[2] ILA_5150 GmbH, Rotter Bruch 26a, 52068 Aachen, Germany

Published online: 23 February 2023

relative velocities onto smooth, rough or structured surfaces (Rioboo et al. 2001; Yarin et al. 2017). However, these measurements provide only a two-dimensional representation of the drop shape, whereas the drop dynamics are inherently three-dimensional (3D), especially in the non-equilibrium phase of the impact and/or the impact onto non-isotropically structured surfaces.

While numerical simulations can deliver a three-dimensional representation of the droplet (Fink et al. 2018; Wörner et al. 2021), their model functions for the contact angle dynamics rely on measured droplet characteristics from experiments (Kistler 1993; Cox 1986). Furthermore, these simulations have to be validated on adequate experimental data. The validation is rendered difficult due to the lack of an accurate three-dimensional representation of the gas–liquid interface in experimental data.

Various techniques for the volumetric reconstruction of liquid surfaces from experimental data have been developed, including methods based on refraction, diffuse reflection, fluorescence or specular reflection and methods from computer vision that might see an application to fluid measurements in future. Morris and Kutulakos (2011) used the refractive properties of the gas–liquid interface to reconstruct the three-dimensional surface of a fluid film. The authors captured the deformation of a known reference pattern placed below the fluid surface in a stereo setup and subsequently determined the 3D shape by the comparison with a calibration image. Recently, Qian et al. (2017) extended the dynamic-refraction stereo-based approach by further constraining the reconstruction to match the local 3D geometry, which allowed for a more precise estimation of the position and orientation of the surface. Dehaeck et al. (2013) utilized the fringe pattern that is created by the refraction of a liquid droplet imaged from below in a Mach-Zehnder interferometry setup in order to reconstruct the three-dimensional volume by means of a 1D wavelet transform, later expanding their setup for the reconstruction of an asymmetric droplet through 2D fan wavelets Dehaeck et al. (2015).

Conversely, structured light techniques rely on the deformation of a light pattern projected onto the surface of a liquid by the diffuse reflection for a three-dimensional reconstruction. Zhang et al. (2015) determined the thickness of a fluid film through a cross-correlation between the deformed image and a calibration image using a digital image pattern. Hu et al. (2015) applied the Fourier transform profilometry (see Takeda et al. 1982), a method in which a fringe pattern is modulated by the fluid surface, for the volumetric reconstruction of liquid films and the wind-driven droplet flow on an airfoil.

Ihrke et al. (2005) exploited the emission from fluorescent dye dissolved in the fluid imaged from multiple viewpoints for the volumetric reconstruction of a stream of water. More recently, Roth et al. (2020) combined laser-induced fluorescence (LIF) (Kinsey 1977) and the projection of a fringe pattern to reconstruct the 3D-surface of a pendent droplet with a single camera setup. Horbach and Dang (2010) used the reflection of a structured light pattern on a specular surface for a 3D reconstruction through a region-growing approach that considers local curvature features.

A variety of methods for the monocular reconstruction of fluid surfaces from specularity have been developed in the area of computer vision. Li et al. (2013) utilized the shape from shading method (Horn 1970) for the reconstruction of a wavy water surface from specular reflection, followed by a refinement of the reconstructed surface through physical constraints by a shallow water model. Similarly, Yu and Quan (2013) estimated the height of a fluid surface with waves through specular reflection and employed the Stokes wave model in order to improve the accuracy of the reconstruction.

The glare points that result from the scattering of light on a liquid droplet can be used for a measurement of its fluid mechanical properties. König et al. (1986) used the fringe pattern created by the interference of defocused glare points from reflected and refracted light (produced in wide-angle forward scatter) to measure the diameter of droplets. Later, Glover et al. (1995) applied this method to determine the diameter, position and velocity of droplets in a polydisperse spray. Conversely, Dehaeck et al. (2005) used in-focus glare points to measure the size and velocity of bubbles in a fluid flow. The authors encode additional information through an additional reflective glare point produced by a light source at a different illumination angle. This glare point can be used for the detection of non-spherical bubbles and the determination of the relative refractive index between the gas and liquid phases. More recently, Brunel et al. (2021) used interferometric particle imaging (IPI) with three perpendicular views in order to reconstruct the 3D-shape and orientation of irregularly shaped rough particles from their speckle patterns.

For the reconstruction of the three-dimensional shape of deformed droplets or bubbles various multi-view methods based on the shadowgraphy technique have been developed. Honkanen (2009) reconstructed the volume of a bubble from two orthogonal projections in a backlight shadowgraphy setup by the piece-wise fit of ellipses within a 3D bounding box. More recently, Fu and Liu (2018); Masuk et al. (2019) performed a highly accurate volumetric reconstruction of 3D bubble surfaces through the visual hull method (Laurentini 1994) from multiple view angles, followed by a smoothing of the reconstructed volume considering the additional physical constraint of a minimum surface. Ríos-López et al. (2018) reconstructed the three-dimensional shape of a non-axisysmmetrical droplet sliding on a flat surface from two views with the assumption of one symmetry plane.

The above introduced single view methods are in many cases only applicable at a limited degree of surface deformation or curvature, which as yet renders multi-view methods mandatory for any advanced volumetric reconstruction of an impinging droplet. To address this deficiency of single view methods, the present study introduces an optical measurement method based on the shadowgraphy technique, which encodes additional three-dimensional information of the droplet during impact through glare points resulting from differently colored light sources at different scattering angles in the channels of a single RGB image. The thereby acquired additional measurements of the deformed phase boundary during impact lay the ground for a volumetric reconstruction of droplets phase boundary. Moreover, the introduced approach is considered to be straight-forwardly adaptable to other spatio-temporal gas–liquid interface investigations with complex non-trivial interface shape.

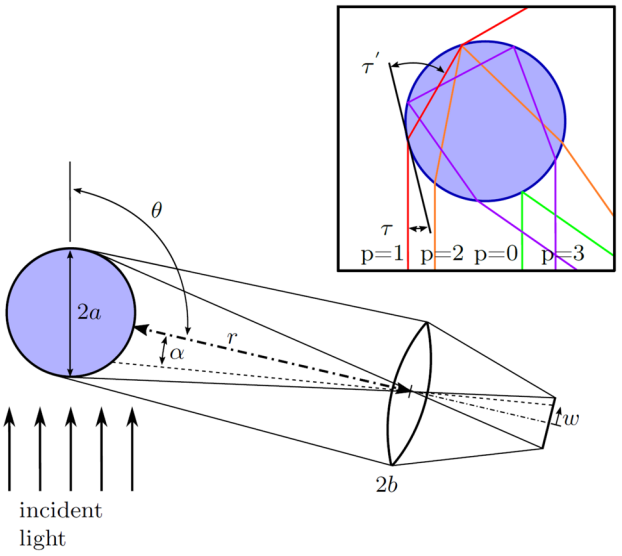

Fig. 1 Geometrical description of the setup required for glare points (adapted from van de Hulst and Wang 1991). Insert: Ray diagram of the first four glare-point orders in geometrical optics for a circular cross section of a water droplet in air. The solid lines indicate visible glare point orders, while dashed lines indicate non-visible glare point orders

2 Methods

2.1 Theory of glare points

The formation and characteristics of glare points in both the theory of geometrical optics (GO) and wave optics (Born et al. 1999) will be briefly recapitulated here in the context of droplets. Glare points are the bright spots on the surface of the droplet that result from the scattering of a wide beam of parallel light according to van de Hulst (1981). In GO, glare points are described as the exit points of light rays that are either reflected or refracted on the surface in the direction of scattering θ (Kerker 1969), as can be seen in Fig. 1. This results in the emergence of different orders of glare points, defined by the chords traveled within the droplet p (Debye 1908), where $p = 0$ indicates the externally reflected light, $p = 1$ the transmitted and twice refracted light rays and $p = 2$ the refracted and internally reflected light rays.

As indicated in Fig. 1 by the parallel $p = 0$ (red) and $p = 3$ (green) rays, multiple orders of glare points can be visible simultaneously for the same scattering angle. Conversely there exist ranges of scattering angles at which certain orders of glare points are not visible at all, as illustrated by the $p = 1$ (orange) ray in Fig. 1. According to van de Hulst and Wang (1991) all relevant rays for the formation of glare points at a perfect sphere propagate within the scattering plane, defined by the direction of the incident light and the scatter direction. Furthermore, the GO theory of glare points is applicable for volumes with a plane of circular cross section and, therefore, to spheroids and cylinders as well. The description of glare points in GO is valid for size parameters $x = (2\pi a)/\lambda \gg 1$, with $2a$ describing the droplet diameter and λ the wavelength of the incident light. This holds true for $2a \approx 2$ mm and $\lambda =$ 400–700 nm in the experiments conducted in the present work.

The required equations for the calculation of the glare point positions in GO will be summarized in the following. The angle between an incident light ray and the surface of the droplet τ can be set in relation to the angle between the refracted ray and the surface τ' according to

$$n_1 \cos(\tau) = n_2 \cos(\tau') \tag{1}$$

considering Snell's law (see e.g. Hecht 2017) with the refractive indices n_1 of the surrounding gas and n_2 inside the droplet.

Considering the possible cases of external reflection, $p - 1$ internal reflections and the refraction of a light ray, the deflection angle θ' can be determined. Subsequently, the scattering angle θ can be calculated to be

$$\theta' = 2(\tau - p\tau') = 2\pi k + q\theta, \tag{2}$$

where k is an integer, depending on the number of internal reflections (van de Hulst 1981, pp.228ff) and $q = \pm 1$, depending on the side of the projected droplet relative to the optical axis, which can be described by the variable $w = \alpha l/a$. This dimensionless quantity w describes the position on the image plane relative to the droplets projection as function of the droplet diameter $2a$, the distance between the lens and the droplet l, and the angle α between the optical axis and the position on the droplet, as seen from the lens

perspective (see Fig. 1). The position of the glare point in the dimensionless coordinate w follows as

$$w = q\cos(\tau). \tag{3}$$

Note that Eqs. 2 and 3 only hold for a spherical droplet. Note, however, that a GO description for non-spherical droplets, which are symmetric around the optical axis was developed by Hovenac (1991).

The scattering angle is non-monotonically dependent on the incident angle for $p \geq 2$. Therefore, $\theta(\tau)$ possesses an extremum at the rainbow angle θ_c (Walker 1976), which can be determined by $\mathrm{d}\theta/\mathrm{d}w = 0$ (van de Hulst 1981). The deflection of the incident light rays θ' is minimal at the rainbow angle and increases toward both larger and smaller scattering angles. As such, the density of the light rays exiting the droplet reaches a maximum at θ_c, which results in the highest scattered intensity at the rainbow angle. The scattering angle θ can either be maximal or minimal at θ_c, depending on the order of the rays p. A further consequence is that no scattered rays beyond the rainbow angle are possible.

Note that the two visible rainbows in nature can be explained accordingly—rays of the order $p = 2$ create the primary rainbow and $p = 3$ rays produce the weaker secondary rainbow above the primary rainbow. Higher orders of rainbows become increasingly dim as their incident angle increases such that less droplet surface is illuminated. Furthermore, the light is partly refracted at every reflection. Due to dispersion, the polychromatic light of the sun is scattered at slightly different angles around the rainbow angle, creating the well known color gradients. For $p = 2$ the rainbow angle is the minimal possible scattering angle and for $p = 3$ it is the maximum scattering angle, which results in inverted color gradients and also explains the appearance of Alexander's dark band between the rainbows in which no light is scattered (Nussenzveig 1977).

The complete description of glare points for arbitrary-sized spheres is given in wave optics through Lorenz-Mie theory, which is the exact solution for the problem of light scattering on a spherical particle (Mie 1908). van de Hulst and Wang (1991) derive the equation for the amplitude of the glare points with the following assumptions. Firstly, a well defined scattering plane, that contains the direction of incidence and the direction of scattering is assumed. Consequently, the scattering plane excludes the $\theta = 0°$ and $180°$ scattering angles. Secondly, the authors assume that the lens both follows the thin lens equation (Hecht 2017) and is placed in the far field. The glare point equation accordingly follows as

$$A_{\parallel\perp}(w) = \int_{\theta_0 - b/l}^{\theta_0 + b/l} S_{\parallel\perp}(\theta) \exp\left[-ixw\left(\theta - \theta_0\right)\right] \mathrm{d}\theta, \tag{4}$$

in which $S_{\parallel\perp}(\theta)$ is the electrical field amplitude of the scattered light, θ_0 is the scattering angle and $2b$ is the diameter of the lens. $S_{\parallel\perp}(\theta)$ represents either parallelly $S_{\parallel}$ or perpendicularly $S_{\perp}$ polarized light. Consequently, the size of glare points arising from a plane wave impinging on the droplet will depend on the size (and shape) of the receiving aperture. The expected amplitude of the scattered light following Eq. 4 for the combination of all glare point orders can be seen in Fig. 10. A comprehensive derivation of the scattering on spherical particles is provided in the treatise of van de Hulst (1981).

2.2 Experimental setup

The present approach extends the shadowgraphy method by supplementing two lateral light sources to the standard shadowgraphy setup as shown in Fig. 2. These additional light sources are mounted on a custom-built rail system as can be seen in Fig. 2b in order to allow for the adjustment of the azimuth angle θ, while the elevation angle Φ can be adjusted by a hinge. This mounting system facilitates the independent and continuously variable adjustment of both angles and, thereby, allows for the evaluation of the influence of the direction of illumination on the glare-point location and intensity on the gas–liquid interface. The angular adjustment uncertainty is estimated to be lower than $\pm 2°$. In order to ensure a reproducible droplet volume over multiple experiments and to avoid oscillations of the droplet from the introduction of momentum, the water droplet is produced by an automatic drop-application system. This system consists of a syringe with a cannula diameter of $d_s = 0.1$ mm and a

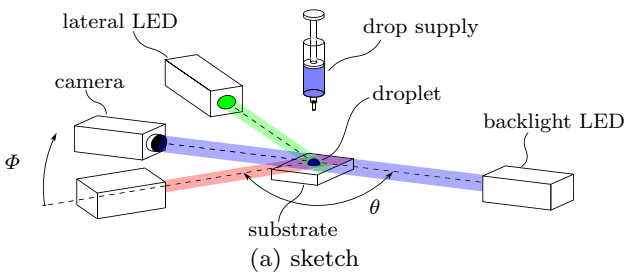

(a) sketch

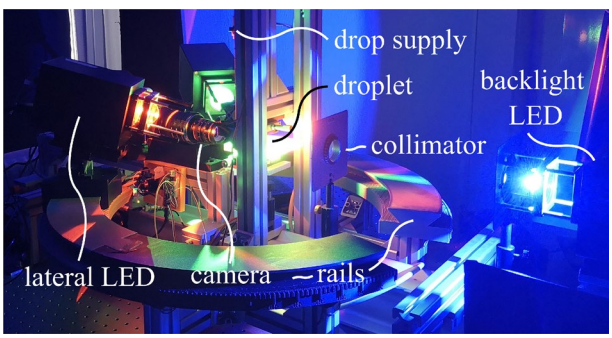

(b) photograph

Fig. 2 Sketch (**a**) and photograph (**b**) of the experimental setup of the applied RGB-shadowgraphy method

stepper motor with $l = 10$ mm linear displacement and a step angle of $\alpha = 7.5°$, which is used as a linear actuator for the syringe. The resulting droplet diameter for distilled water is $2a \approx 2$ mm at room temperature. The considered substrate has a hydrophobic surface created by a silicon oxide (SiOx) coating.

The two lateral light sources, as well as the backlight are high-power *ILA_5150 LPSv3* LEDs with narrow-banded spectra and maxima in the visible spectrum at ~ 455 nm ("*blue*"), ~ 521 nm ("*green*") and ~ 632 nm ("*red*") for the desired blue, green and red light sources, respectively. The light of the LEDs is captured either at 3,000 frames per second (fps) by a *Photron Fastcam Mini WX* RGB-Camera or at 7,500 fps by a *Photron Nova R2*, both equipped with a *Schneider-Kreuznach Apo-Componon* 4.0/60 enlarging lens, where the three-colors $i =$ ("*red*", "*green*", "*blue*") of illumination are expected to be mainly captured with the corresponding channels of the RGB camera chip.

The backlight produces a classical shadowgraphy image on the corresponding image channel, where only non-deflected light reaches the camera chip. In order to capture the shape of the droplet as accurately as possible a parallel light beam is required, leading to a better resolution of small features and optimizing contrast (Settles 2001). This is achieved by placing an optical collimator consisting of a pinhole aperture with a diameter of $d_a = 4$ mm and a *Spindler & Hoyer* biconvex collimator lens with 300 mm focal length between the backlight and the droplet. The blue LED is used for the backlight, since the camera chip possesses the lowest relative sensitivity in this range of wavelengths and the highest response in the chip is expected from direct illumination of the backlight LED.

The lateral light sources are focused by *Thorlabs* plano-convex lenses with a broadband anti-reflective coating (reflectivity $< 0.5\%$) and illuminate the droplet from an azimuthal angle $\theta > 90°$ in respect to the blue LED. Consequently, only reflected light reaches the camera, resulting in the creation of $p = 0$ glare points (van de Hulst and Wang 1991). The illuminating light beams possess a cross section that is larger than the droplet and are approximately parallel, which implies that the beams can be represented as plane waves. Since the light is partially transmitted at the first interface between air and water, it is reflected again on the following interfaces in the path of the light ray, e.g. while leaving the droplet or at internal phase boundaries of air inclusion within the droplet, resulting in higher order glare points ($p \geq 2$).

Due to the smooth surface of the phase boundary, pure interface reflection is considered, which is captured by the camera as differently colored glare points on each side of the droplet and on any present air bubbles, thereby encoding additional volumetric information on the droplet in the remaining red and green image channels. Since the information is separated between the channels of the RGB-image, three individual grayscale images with accordingly different illumination conditions can be extracted from the RGB-image, each providing a unique representation of the droplet that can be used for the volumetric reconstruction of the droplet.

2.3 Data processing and spectral reconstruction

The spectral power distribution of the light sources do not perfectly match with the spectral sensitivity of the corresponding camera channels $k =$(R, G, B) as illustrated in Fig. 3. Therefore, each light source causes a perturbation of the images in the other channels, which consequently needs to be considered as follows.

The response of the kth color channel at pixel x on the camera chip $I_k(x)$ can be calculated by spectral integration from the spectral power distribution (SPD) of the incoming light $L(\lambda)$, the spectral transmittance of the color filter $T_k(\lambda)$ for the kth color channel and the spectral responsivity $s(\lambda)$ of the camera (Shafer 1982) as

$$I_k(x) = \int_\lambda L(\lambda) T_k(\lambda) s(\lambda)\, \mathrm{d}\lambda. \tag{5}$$

Equation 5 implies the assumption of a linear camera-chip behavior, i.e., the measured signal at a pixel's location x is proportional to the intensity of the incident light at this position. This assumption generally holds true, however, with little error for CMOS cameras (Wang and Theuwissen 2017). The spectral transmittance $T_k(\lambda)$ and the spectral responsivity of the camera $s(\lambda)$ are often expressed in a combined form as the spectral sensitivity of the camera $S_k(\lambda) = T_k(\lambda)s(\lambda)$ for the kth color channel. The term of the camera's spectral sensitivity $S_k(\lambda)$ also includes the wavelength-dependent transmittance of the objective lens $T_o(\lambda)$, while the transmittance of the focusing lenses of the light

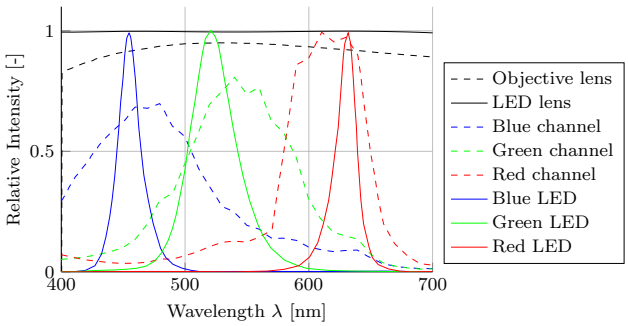

Fig. 3 Spectral power distribution of the LED light sources (color-coded solid lines); spectral sensitivity distribution of the camera's color channels k (color-coded dashed lines); transmittance of the objective lens (dashed black line) and the collimator lenses of the light sources (solid black line)

sources can be assumed to be constant in the relevant wavelength-band, as seen in Fig. 3. Since spectral integration is a linear transformation, an integration over $L(\lambda)$, which is the combined superposed spectral power distribution of all light sources i via $L(\lambda) = \sum_{i=1}^{n} \int_{\lambda} L_i(\lambda)$, results in the same camera response as the sum of an integration over all light sources $L_i(\lambda)$ (Klinker et al. 1988). Therefore, Eq. 5 can be rewritten as

$$I_k(x) = \sum_{i=1}^{n} \int_{\lambda} L_i(\lambda) S_k(\lambda)\, \mathrm{d}\lambda. \tag{6}$$

Considering that light transport from the two lateral light sources to the camera chip can occur either directly or by scattering on the droplet, thus creating glare points, the light transport coefficient $l(\lambda, x)$ at pixel position x on the camera sensor is introduced as

$$I_k(x) = \sum_{i=1}^{n} \int_{\lambda} l_i(\lambda, x) L_i(\lambda) S_k(\lambda)\, \mathrm{d}\lambda. \tag{7}$$

In order to consider the contributions of direct illumination, reflection at the droplet interface and transmission through the droplet, the light transport coefficient is expressed as

$$l(\lambda, x) = d(x) + r(\lambda, x) + t(\lambda, x) \tag{8}$$

where $d(x)$ represents the direct light transport, $r(\lambda, x)$ the spectral reflectance and $t(\lambda, x)$ the transmission. Generally, spectral reflectance and transmission are dependent on direction and wavelength of the light incident on the surface and the geometrical shape of the illuminated object, whereas the participation from direct light only depends on the illumination angle. Furthermore, the spectral reflectance can be divided into interface (specular) reflection $r_s(\lambda, x)$ and body (diffuse) reflection $r_d(\lambda, x)$, according to the dichromatic reflection model (Shafer 1984), i.e.,

$$r(\lambda, x) = r_s(\lambda, x) + r_d(\lambda, x). \tag{9}$$

For a water droplet, the diffuse reflection $r_d(\lambda, x)$ is neglected due to the smoothness of the surface, so that reflection can be assumed to be only specular reflection $r_s(\lambda, x)$ in the following.

The light transport by transmission $t(\lambda, x)$ is determined by the two-fold refraction at the droplet interface $r_f(x, \lambda)$ and the spectral transmittance $T_D(x, \lambda)$ of the droplet liquid. Following the Beer-Lambert law (Swinehart 1962), the absorption of distilled water in the visible spectrum is negligibly low for the considered distance traveled within the droplet (Hale and Querry 1973), even considering longer distances for higher order glare points. Therefore, the spectral transmittance can be considered to be $T_D \approx 1$ in the range of the considered wavelengths ($\lambda \approx 400 - 700$ nm) and its influence on the light transport trough transmission can be neglected.

Interface reflection and refraction are in general dependent on the refractive index n following the Fresnel equations (Hecht 2017). Since n is furthermore dependent on the wavelength of the incident light, i.e., $n = n(\lambda)$, the intensity of both reflected and transmitted light on the interface likewise depend on the wavelength. Note that the light of the LEDs is unpolarised. Therefore, in the following the effects of polarisation on the reflection are not considered.

The neutral interface reflection (NIR) model is a good approximation for a water droplet. It states that the spectral power distributions (SPD) of the reflected and incident light are approximately equal (Lee et al. 1990). This assumption is valid for materials with insignificant variation of refractive index in the visible spectrum, which holds true for water. With the assumption of dominating specular reflectance and the NIR model the spectral reflectance r becomes independent from the wavelength, i.e., $r(x) = r_s(x)$. Furthermore, for $n \approx const.$ the refraction becomes independent of the wavelength $r_f(x)$. Consequently, the light transport only depends on the geometry of the problem $l(x)$ and Eq. 7 can be accordingly rewritten as

$$I_k(x) = \sum_{i=1}^{n} l_i(x) \int_{\lambda} L_i(\lambda) S_k(\lambda)\, \mathrm{d}\lambda. \tag{10}$$

Since both the SPD of the light sources and the spectral sensitivity of the camera are known, an integration across all relevant wavelengths for the camera sensor results in a transfer coefficient

$$t_{k,i} = \int_{\lambda} L_i(\lambda) S_k(\lambda)\, \mathrm{d}\lambda \tag{11}$$

to quantify the transfer of light from each light source L_i to each channel of the camera chip I_k.

For the presented measurement setup, consisting of three LEDs with different maximal wavelengths in the red, green and blue spectral range of the visible light (L_r, L_g, L_b), and a camera chip with a red, a green and a blue channel (I_R, I_G, I_B), the resulting transfer function is represented by

$$\begin{pmatrix} I_R \\ I_G \\ I_B \end{pmatrix} = \begin{pmatrix} t_{Rr} & t_{Rg} & t_{Rb} \\ t_{Gr} & t_{Gg} & t_{Gb} \\ t_{Br} & t_{Bg} & t_{Bb} \end{pmatrix} * \begin{pmatrix} l_r \\ l_g \\ l_b \end{pmatrix} = \mathbf{T} * \mathbf{l}. \tag{12}$$

Finally, the inverse of the transfer matrix $\mathbf{T}$ provides a correction matrix $\mathbf{C} = \mathbf{T}^{-1}$ for a determination of the image $\mathbf{l}$

created as a result of the light transport from only a singular light source

$$\mathbf{I} = \mathbf{T}^{-1} * \mathbf{I} = \mathbf{C} * \mathbf{I} \tag{13}$$

from the response of the three image channels **I**. Therefore, the analytical spectral correction (ASC) function 13 allows for a separation of the images created by each only one of the light sources, resulting in three independent images of the droplet.

The transfer coefficients in Eq. 12 and thus the correction matrix can also be obtained in-situ from the experimental apparatus by means of calibration images, in the following called in-situ color correction (ISC). ISC is particularly useful if the spectral characteristics of the optical components are unknown and, consequently, ASC cannot be applied. For this purpose three sets of calibration images have to be recorded in the presented setup through an RGB-camera, where consecutively only a single light source L_i is active per recording. Afterward the channels I_k of the RGB-images are split from each other to achieve nine grayscale images that contain the required information to calculate the transfer coefficients $t_{k,i}$ of Eq. 12. An accurate estimate for the transfer coefficients can be obtained by calculating the maximum channel intensities and averaging over a large set of calibration images, thus reducing the influence of random noise. While ISC proved to be effective, additional measurement errors have to be considered in comparison with the above-introduced analytical method.

3 Results

3.1 Results of spectral reconstruction

The images of a water droplet impinging onto a flat substrate recorded for the present work with the above-introduced RGB shadowgraphy setup and their processing are discussed in the following section. The required information for the ASC function 13 is calculated from the SPD of the LED lights and the spectral sensitivity of the camera with the values provided by the manufacturers; see Fig. 3.

Figure 4 shows an RGB frame of the droplet shortly after impact and the separated response of the uncorrected channels of the raw image. The comparison of the three separate image channels to the RGB image demonstrates that the additional information from reflective images of lateral light sources of different wavelength bands can be separated into the channels of an RGB image, which however contain some spurious crosstalk between the images. Saliently, the background of the green channel is considerably illuminated by the blue light source and the reflective images from the lateral light are apparent on the other channels, but with a lower intensity. The annotations in Fig. 4b–d highlight the most noticeable perturbations in the respective color of the causative light source.

To reduce the cross-talk effect, the above-discussed ASC function 13 has been applied to the RGB image of Fig. 4. The results are shown in Fig. 5 below the raw

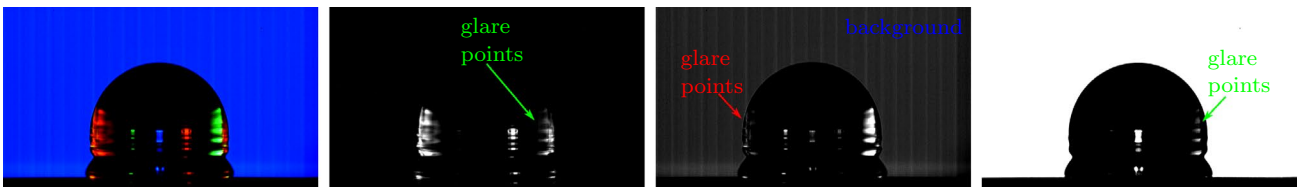

(a) RGB image (b) red (raw) (c) green (raw) (d) blue (raw)

Fig. 4 Raw color-imaging of an impinging water droplet on a substrate with SiOx-coating; **a** RGB snap shot; separated **b** red, **c** green and **d** blue raw channels of **a**. The color-coded annotations highlight the perturbations from the respective other channels

(a) RGB image (b) red (corrected) (c) green (corrected) (d) blue (corrected)

Fig. 5 Processed color-imaging of an impinging water droplet on a substrate with SiOx-coating; **a** RGB snap shot; separated **b** red, **c** green and **d** blue corrected channels of (**a**)

images to allow an immediate comparison of all spurious patches. Obviously, most disturbances in Fig. 4 have been successfully removed or at least reduced significantly. This is most saliently emphasized by the removal of the background light in the green channel and the transmitted light around the vertical center line resulting from the blue light source. The glare points from the red light source on the right side of the droplet in the green image are reduced as well. In the blue and red channels the glare points from the green light source on the left side of the droplet are likewise removed successfully. The full series of RGB frames shortly before and after the drop impact, corrected with the ISC function, is provided in Appendix 1 to further contrast the raw images (Fig. 19) to the corrected images (Fig. 20).

A quantitative accuracy evaluation of the image color correction has been conducted on images from the RGB imaging with only one activated light source. In this setup a complete color correction is expected to result in zero intensities for all but the considered image channels and only the channel corresponding to the active light source is expected to contain an image. The quality of the color correction is measured by the mean image intensity in the omitted image channels, i.e., the remaining disturbance after correction. Figure 6 shows the temporal evolution of mean image intensities for all channels in the first 50 images of the drop impact before (dashed lines) and after (solid lines) color correction.

As expected, each light source causes the highest response in the corresponding image channel and additionally a smaller response in each of the two other channels. The intensity of the disturbance in the omitted channels is significantly reduced by the color correction, as becomes obvious from the reduction of average intensity for the respective channel to near-zero values for most frames. This evaluation, therefore, confirms the accuracy of the applied analytical color-correction approach. While the correction of the blue light is nearly perfect, the disturbance in the other channels cannot be fully eliminated for particular frames recorded with only the lateral green or red light source. The corresponding frames are characterized by high overexposure, such that clipping effects lead to an effective overestimation of the other channels. One such event is shown in Fig. 7, which occurred in the 38th frame of an RGB shadowgraphy experiment with only the green lateral light source activated (cp. Fig. 6b, where the considered frame is marked with a black arrow).

3.2 Glare point prediction accuracy

To evaluate the accuracy of the recorded glare-point locations and intensities, the occurrence of the glare points in

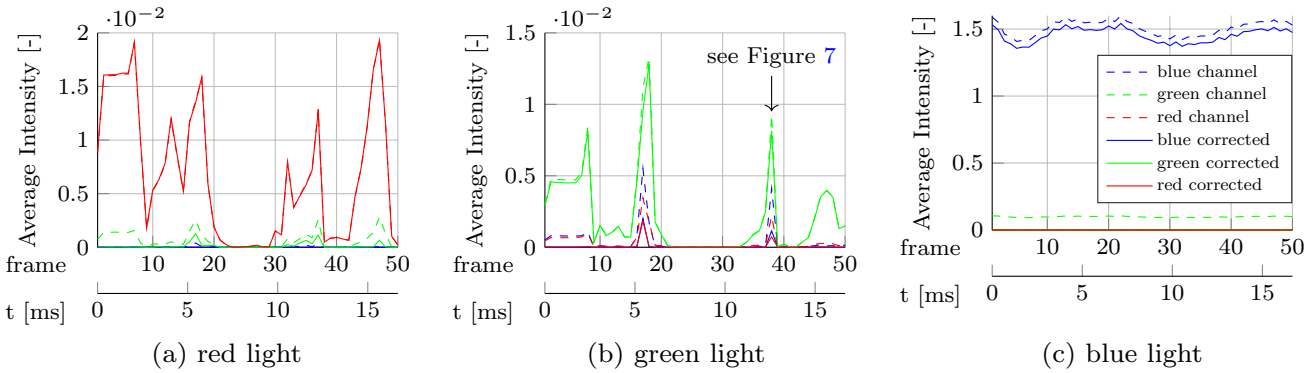

Fig. 6 Mean image intensities of the unprocessed color channels (dashed lines) in comparison with the ASC-corrected color images (solid lines) for the first 50 frames of the drop-impact measurements with a single lateral red (**a**), green (**b**) light source or blue backlight (**c**)

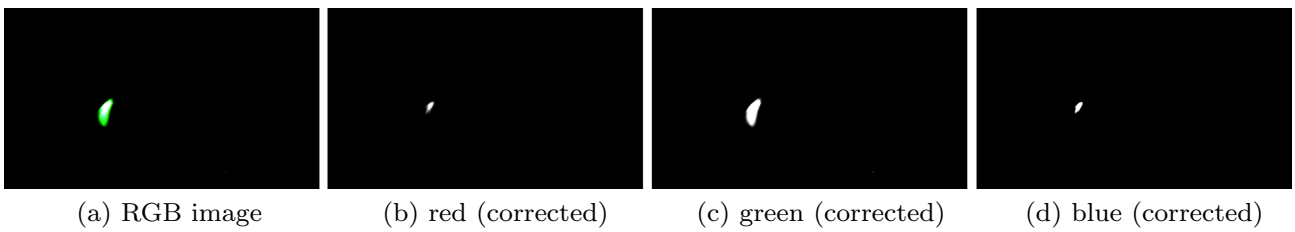

Fig. 7 Processed color-imaging with overexposure (frame 38), produced with only the green lateral light source activated; **a** RGB snap shot; separated (**b**) red, **c** green and **d** blue corrected channels of (**a**)

the experimental images is compared to the theoretically expected results as can be calculated from the Lorenz-Mie theory for scattering on a spherical particle with Eq. 4. In the following the glare-point position is defined by the location of the maximum glare-point intensity. First, the position of the glare points on the projected gas–liquid interface of the droplet, as well as their relative intensity is evaluated for the simple case of a spherical droplet illuminated at $\Phi = 0°$ elevation angle. The azimuth angle is varied from $\theta = 95°$ to 145° in increments of 10°, which corresponds to the angular range for which back-scattering occurs and that was simultaneously possible with the presented experimental setup. A corresponding set of recordings is shown in Fig. 8, where only the red channel appears as gray scale images. To guide the unaided eye, the uncorrected image channel with e.g., spurious backlight is shown, even though the corrected image channels were processed and are discussed below.

Figure 9 shows the column-wise averaged intensity of the red image channel after applying the previously introduced ISC method, therefore revealing the distribution intensity of the glare points over the projected gas–liquid interface of the droplet. The column-wise intensity was calculated for five rows of the color-corrected image around the maximum horizontal expanse of the droplet and subsequently averaged over five frames. Note that the third (center) frame of this temporal average corresponds to Fig. 8. The reconstructed glare point signal allows for a comparison of the position of the glare points in the experiment to the position expected from the calculations by van de Hulst and Wang (1991) following Eq. 4, shown in Fig. 10.

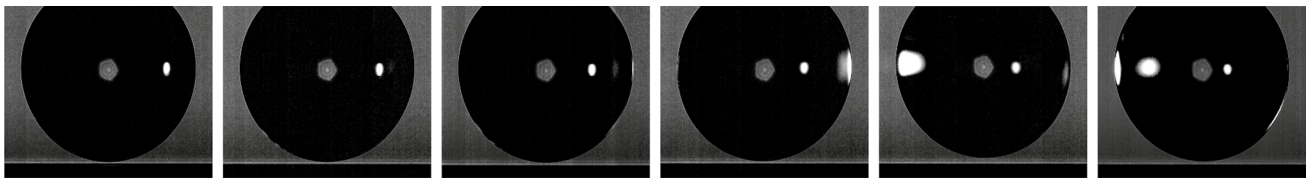

Fig. 8 Red image channel of the frame with a spherical water droplet before impact for different azimuth angles θ. The identical order of angles is found in Figs. 9 and 10. The uncorrected channel was chosen for the better visibility of the droplet contour. (Note that the $p = 1$ glare point from the blue backlight is visible in the center of the droplet due to cross-talk of the camera and has the same intensity as the background)

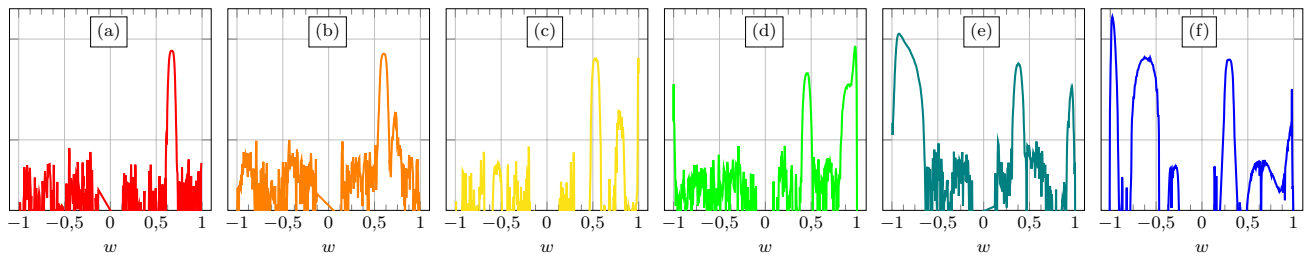

Fig. 9 Glare-point intensity measured from the ISC corrected red channel from a recording of a spherical droplet in the experiments. The column-wise averaged glare point intensity is plotted on the logarithmic ordinate against the dimensionless variable w on the abscissa, that describes the position on the scattering plane relative to the projection of the droplet, as introduced in Sect. 2.1

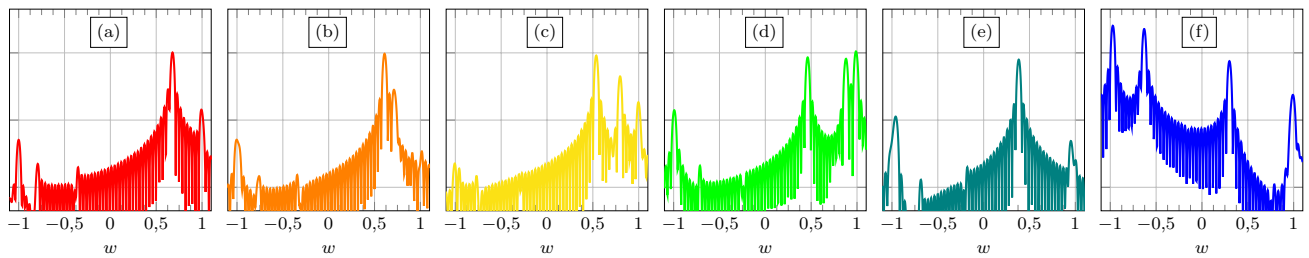

Fig. 10 Mie glare-point images calculated by means of Eq. 4. The logarithmic glare-point intensity is plotted on the ordinate against the dimensionless variable w on the abscissa

The good agreement of the position of the glare-point peaks in the experimental images and the theoretically expected intensities allows for an interpretation and subsequent differentiation of the contributing orders in the observed glare-point signal from the experiment. In Fig. 9a only the zeroth order glare point ($p = 0$) is clearly visible at around $w = 0.67$, which is in good agreement with the theoretically expected position. Toward higher scattering angles the zeroth order glare point moves toward the center of the droplet and reaches $w = 0.29$ at 145°, as can be seen in Fig. 9f. The exact glare point positions in geometrical optics are calculated by Eq. 2 and subsequently Eq. 3 for further comparison. The results showed a good agreement with the experimentally determined positions.

In Fig. 9b additionally a third order glare-point peak ($p = 3$) becomes visible at $w = 0.73$, despite the order-of-magnitude difference in intensity to the main peak. The comparison of the predicted intensity with the measured signal confirms the presence of a third order peak to the right of the strong zeroth order peak (cp. Fig. 10b). The intensity of the third order glare point increases toward higher scattering angles as it approaches its rainbow angle at 129.5°. In Fig. 9c the third order glare point is clearly visible at $w = 0.8$. The theory predicts a second third order glare point at the $w = 1$ edge of the droplet that can be confirmed by a clearly visible intensity peak in the experiment. Both third order glare points are predicted to merge into a single, bright glare point at their rainbow angle, as can be seen in Fig. 18b. However, in Fig. 9d they can still be clearly differentiated at a scattering angle of 125° as evident from the experimental image and the corresponding intensity curve.

A second order glare point ($p = 2$) first emerges in Fig. 9e as a large and bright glare point around $w = -0.92$. Since the scattering angle lies close to the second order rainbow angle of 137.7°, the intensity of the glare points is high. In Fig. 9f two second order glare points are visible at $w \approx -0.61$ and close to the edge. As predicted by theory, the second order glare point, therefore, behaves in the opposite way as the third order glare point and splits into two peaks for scattering angles larger than the rainbow angle. The comparison of the measured and computed glare points close to the $p = 2$ rainbow angle (see Fig. 18c) reveals, that in fact the scattering angle in the experiments has been closer to 137.7° than 135.0°, as the expected relative intensity peaks produce a better match. This elucidates that the intensity of the glare points close to their respective rainbow angles reacts sensible to small angular changes. However, the position of the glare points does not change significantly, therefore allowing for an accurate prediction of glare point occurrence by Eq. 4.

The first order glare point ($p = 1$) was not visible in the range of evaluated azimuthal angles θ, as it appears only at scattering angles smaller than 82.6° according to geometrical optics and following Eq. 2. In a similar manner the intensity of the fourth and fifth order glare points is predicted to be too low to result in visible glare points, which is confirmed by the experimental results. Higher order rainbows accumulate at the $w = \pm 1$ edges, resulting in intensity peaks from potentially multiple higher order glare points, complicating the interpretation of the edge peaks. Furthermore the higher order glare points become increasingly more sensible to deviations in the scattering angle, since the greater number of internal reflections amplify any deviation. Therefore, the interpretation of higher order glare points becomes less reliable.

According to van de Hulst and Wang (1991) additionally surface waves might contribute to the edge peaks as well. However sixth ($p = 6$) and seventh order glare points ($p = 7$) appear plausible following the descriptions of van de Hulst and Wang (1991). The intensity peak at the $w = -1$ edge in Fig. 9d, e matches the theoretical position of the sixth order glare point, while in Fig. 9e, f the peaks at $w = 0.96$, respectively at $w = 0.98$ match the expected seventh order glare point. Additionally, the diffraction on the droplet is visible around the contour of the droplet in all images, contributing to all the glare point signal in Fig. 9 and in particular at the edges.

It should be noted that according to Walker (1976) the rainbow angle calculated in wave optics differs by ≈ 0.15° for $p = 2$ and ≈ 0.21° for $p = 3$ in comparison with geometrical optics. The resulting deviation in the $p = 3$ glare-point position was calculated to be $\delta_w < 0.0005$, which is considered negligible. The angular difference for the $p = 2$ rainbow angle was even lower, which further confirms that the theoretical calculation provides a valuable and meaningful comparison with the experimentally observed glare points.

3.3 Influence of the elevation angle

To further study the influence of the elevation angle of the lateral light sources on the visibility of glare points on the deforming droplet during impact, the lateral light sources were successively raised and simultaneously tilted in order to illuminate gas–liquid interface from different angles, as sketched in Fig. 2. The elevation angle was varied in a range of $0° \leq \Phi \leq 45°$ with increments of 15° and the additional angle of $\Phi = 50°$, while the azimuth angle was varied from $\theta = 95°$ to 145° with 10° increment. A drop impact experiment with the same kinematic boundary conditions was recorded for each possible combination of elevation and azimuth angles. The images from the experiments were post-processed with the previously introduced ISC in order to obtain the undisturbed glare point images. Figure 11 shows the development of the glare points for experiments performed at 95° azimuth angle in comparison between $\Phi = 0°$ and $\Phi = 45°$ elevation angles by the mean intensity of the color-corrected red and green image channels.

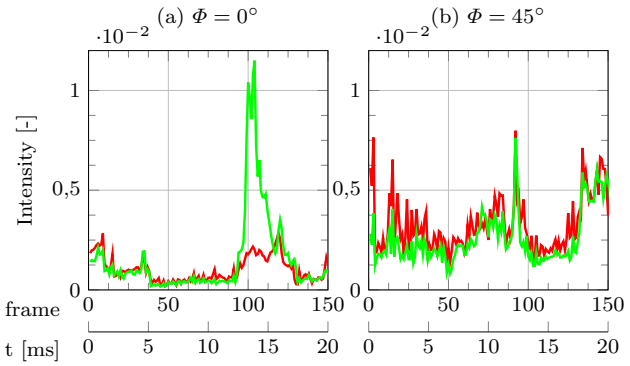

Fig. 11 Mean image intensities of the color-corrected red and green image channels for the first 150 frames of the drop impact; **a** $\Phi = 0°$ elevation angle and **b** $\Phi = 45°$ elevation angle of the lateral light sources

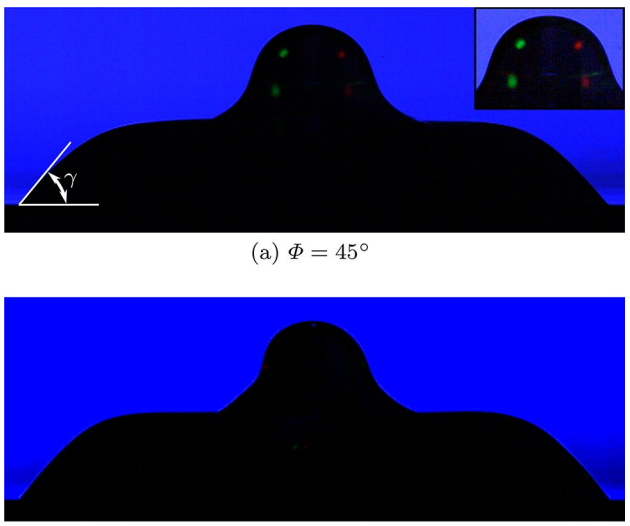

(a) $\Phi = 45°$

(b) $\Phi = 0°$

Fig. 12 Frame with the lowest glare point intensity (frame 50) at an elevation angle $\Phi = 45°$ (**a**) in comparison with a frame for a similar physical time at $\Phi = 0°$ (**b**). The insert in **a** is a contrast-enhanced and brightened repeat of the droplet tip to emphasize the occurrence of glare points

The comparison of Fig. 11a, b provides evidence that the glare-point intensity fluctuates significantly more at the lower elevation angle of $\Phi = 0°$ with some frames reaching close to zero intensity, thus indicating that no glare points were visible in these frames. Such low intensity frames were already apparent in previous experiments at $\Phi = 0°$ elevation angle in which only the lateral light sources were active, as can be seen in Fig. 6. At higher elevation angles, in contrast, significantly more frames contained glare points and the development of the intensity between the frames was more consistent as well. This effect increased toward 45°, after which no further improvement was observed. Figure 12 shows the least luminous frame in the experiments at $\Phi = 45°$ elevation angle (Fig. 12a) and in comparison a frame at $\Phi = 0°$ (Fig. 12b) for a similarly shaped droplet.

As evident from the images at $\Phi = 45°$ elevation angle even the least luminous frame contains clearly visible glare points although faint, as opposed to $\Phi = 0°$ where no glare points are visible. This implies that glare points must be visible in all other frames, which was confirmed by visual inspection. At the chosen azimuth angle of $\theta = 95°$, as expected from the results of Sect. 3.2, only zeroth order glare points appear independent from the elevation angle. Analogous results were obtained for both the intensity and consistency of the glare points at all other azimuthal angles tested in the experiments, including those that resulted in higher-order glare points. For elevation angles larger than $\Phi = 0°$, however, no higher order glare points were observed after a certain deformation of the droplet due to the interaction of the light with the substrate after drop impingement.

4 Discussion

The measurement for glare-point images on the deforming gas–liquid interface with consistent scatter intensity throughout the recorded frames of the drop-impact dynamics is important for a seamless surface reconstruction. As such, the observations and insights of the previous sections will be conflated in order to identify the optimal viewing angles for the lateral light sources below. Further evaluation of 3D-encoding options and limitations follows in the subsequent sections.

4.1 Optimal position of the lateral lights

Figures 4, 5 and 8 indicate that the zeroth order glare points appear only at locations on the surface of the droplet that align with the complementary angle $\Phi_c = 90° - \Phi$ to the direction of the incoming light as viewed from the image plane. In general, the phase boundary of the droplet takes any angle that ranges between the contact angle at the contact-line position and 0° degrees at the top of the droplet. Higher angles are possible due to the deformation of the droplet, as can be seen for example in Fig. 12, but do not necessarily occur. If the contact angle does not exceed the complementary angle to the direction of the incident light, accordingly, frames with no visible glare points might be produced. Consequently, those frames lack the desired additional three-dimensional information of the gas–liquid interface.

The completely horizontal setup with $\Phi = 0°$ elevation angle reveals various frames without glare points for the stages of the drop impact while the contact angle drops

below 90°, which becomes obvious e.g., in Fig. 12. To guarantee the consistent occurrence of glare points, the complementary angle has to remain below the expected range of dynamically varying contact angles in the experiment. Therefore, an elevation angle of $\Phi = 90° - \gamma_r$ is required, in which γ_r is the minimum receding contact angle observed in the experiments (cp. also Fig. 12). Thus, the optimal elevation angle lies within the range between 0° and the minimum receding contact angle γ_r and immediately relies on the wettability of the substrate. Conversely, an increase in the elevation angle leads to a decrease in the distance between the zeroth order glare points, which in turn results in a larger relative measurement error of the distance between the glare points. The theoretical optimum for the elevation angle, therefore, is the lowest angle at which glare points are still visible on all frames during impact. An equilibrium contact angle of $\gamma = 80°$ and a receding contact angle of $\gamma_r = 66°$ characterizes the considered water-droplet impact experiment onto a SiOx-substrate. For this configuration, an elevation angle of 45° was found to produce the most continuous glare point signal.

At elevation angles larger than 0°, higher order glare points mostly disappear as the light that is refracted while entering the droplet interacts with the substrate surface instead of reflecting on the second gas–liquid interface of the droplet. Furthermore, the position of the higher order glare points and the light reflected from the substrate surface quickly become chaotic when the shape of the droplet deviates significantly from the spherical shape. Both of these effects render an interpretation of higher order glare points at elevation angles larger than 0° difficult, as the glare point positions become ambiguous. Combined with the aforementioned requirement for elevation angles $\Phi > 90° - \theta_{rec}$ for a continuous glare point signal—and in particular for hydrophilic substrates—this leaves the zeroth order glare points as the best option for encoding the droplets shape. The restriction to the zeroth order glare point yields the additional benefit of a straight-forward description of the underlying physics and interpretation of the results.

The optimal azimuth angle consequently is the angle at which only the zeroth order glare point is visible. According to GO a scattering angle of $\theta = 96.5°$ leads to the strongest intensity of the zeroth order glare point relative to all other glare points at a wavelength of $\lambda = 632$ nm. At this angle the glare points of orders $3n, n \in \mathbb{N}_0$ coalesce, with the rays forming an equilateral triangle in the droplet, as can be calculated by Eq. 2. The $p = 1$ and $p = 2$ glare points do not appear at $\theta = 96.5°$, as the $p = 1$ rays are limited to $\theta < 82.6°$, which is the angle of the edge ray. Likewise, the $p = 2$ rays are limited to $\theta > 137.7°$, which is the rainbow angle.

Since higher order glare points quickly become less intense outside of a limited range close to their rainbow angle, these orders can be neglected as well. Therefore, $\theta = 96.5°$ can be regarded as a scattering angle that only yields zeroth order glare points. The theoretical derivation above matches well with the experimental results at $\theta = 95°$ azimuth angle (see Fig. 8), which was sufficiently close to the optimal azimuth angle to only produce visible zeroth order glare points. Furthermore, the comparison of the theoretically expected glare points for $\theta = 95.0°$ and 96.5° (see Fig. 18a) reveals that the difference in the intensity distribution is negligibly small. This high tolerance for angular misalignment in turn facilitates a robust, straight-forward calibration of the experimental setup.

The mild influence of the wavelength-dependent refractive index $n(\lambda)$ of water becomes obvious from the above discussion for red light ($\lambda_R = 632$ nm) in comparison the the green light ($\lambda_G = 521$ nm) of the second lateral light source. Accordingly, the green glare points are determined to occur at an optimal angle of $\theta_G = 96.3°$ by Eq. 2. This color-dependent 0.2° difference, however, can be considered negligible in comparison with the angular alignment accuracy of the measurement setup.

4.2 Encoding of 3D-information

In the following section the informative value of the glare points regarding the three-dimensional shape of the droplet will be analyzed. For this purpose a render pipeline for the generation synthetic images was set up in the 3D rendering software *Blender* (Blender Online Community 2018) in combination with the ray-tracing library *LuxCore* (Bucciarelli et al. 2018), which allows to create realistic images of arbitrary droplet geometries that closely match the experimental images.

In order to evaluate the evolution of the glare-point images for non-axisymmetric droplets, ellipsoidal cap geometries with varying aspect ratios were produced by stretching the geometry of a gas–liquid interface extracted from a numerical simulation along one axis in the horizontal plane by factors of $A = 1.0$ to $A = 1.4$ with increments of 0.05. Finally the render setup, configured with an azimuth angle of $\theta = 95°$ and an elevation angle of $\Phi = 45°$ was used to render glare-point images from the droplet geometries at different rotation angles. The renderings created by the aforementioned render pipeline can be seen in Fig. 13 for the aspect ratio $A = 1.25$.

Figure 14a shows the geometrical description of the ellipsoidal droplet that has the aspect ratio$A = \|\mathbf{f}_1\|/\|\mathbf{f}_2\|$ and is rotated by φ relative to the space-fixed frame of reference. Fig. 13a, e shows the geometry rotated by $\varphi = 0°$ and 180°, so that the major axis of the ellipsoid is pointing toward the observer. In order to emphasize the differences between the rendered glare point images at different φ all images in Fig. 13 contain the contour of the $\varphi = 0°$ droplet and the

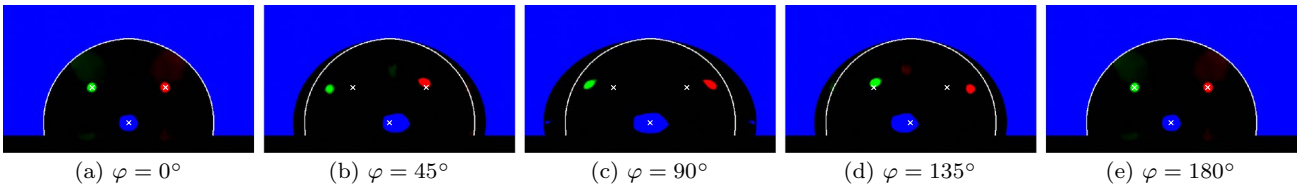

Fig. 13 Renderings of an ellipsoidal cap with an aspect ratio of $A = 1.25$. The droplet is rotated in clockwise direction from **a** to **e**. The images additionally contain the shadowgraph contour (white line) and the glare point positions (white crosses) from the $\varphi = 0$ orientation for comparison

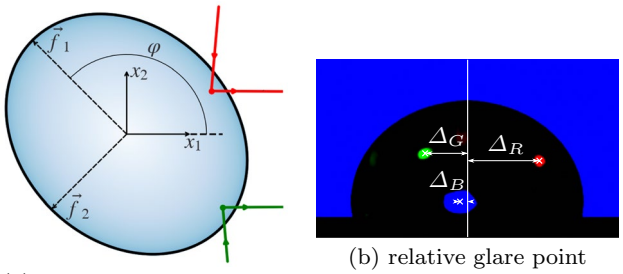

(a) geometrical description (b) relative glare point position

Fig. 14 Geometrical description of the aspherical droplet (**a**) and definition of the glare point positions Δ_R, Δ_G and Δ_B relative to the symmetry axis of the shadowgraph contour (**b**)

positions of the glare points marked by white crosses. The relative position of the glare points in dependence of φ and A was measured relative to the center line of the projection, as indicated in Fig. 14b. The measured positions are plotted in Fig. 15a–c for the red and green zeroth order glare points, and the blue first order glare point, respectively. The aspect ratio A appears as family parameter in the diagrams and angle φ is the functional variable.

As can be seen in Fig. 13 the position of all three glare points moves relative to the shadowgraph contour in dependence of the rotational angle φ and the aspect ratio A. The positions of the red and green glare points appear as phase-shifted and mirrored functions, since both glare points are created through interface reflection ($p = 0$). Their location, therefore, depends on the point on the droplets gas–liquid interface that matches the required angle for interface reflection $\theta_S = (180° - \theta)/2$, which is half the angle included between the camera and the respective light source. The relative position of the blue glare point shows a different dynamic, as it arises from the transmission through the droplet with correspondingly two refractions on the gas liquid interface ($p = 1$).

With the assumption that the shape of the droplet can be described as an ellipsoidal cap with two planes of symmetry along the major and minor axis, two parameters—the rotational angle φ and the aspect ratio A—are sufficient to uniquely determine the three-dimensional shape and position of the droplet. As can be seen in Fig. 15, the relative position of the three (color-specific) glare points are three mutually independent families of functions, since their amplitudes as well as the positions of their maxima depend on the aspect ratio. For a given measurement setup that determines the position of the light sources and the volume of the droplet, φ and A can thus be unambiguously determined from the system of the two $p = 0$ glare-point positions. The relative glare-point positions were determined analytically (see dashed lines in Fig. 15) and show a good agreement with the results from the rendering and, therefore, provide further evidence on the applicability of the considered approach. The derivation of the underlying necessary Eqs. 21 and 22 can be found in the Appendix A. The two $p = 0$ glare points obviously encode the location of the droplets phase boundary of the in the object plane and the local orientation at two additional points outside the shadowgraph plane. For the presented setup the local orientation of the gas–liquid interface at the position of the lateral glare points is $\theta_S = 42.5°$ in the azimuth angle and $\Phi = 45°$ elevation angle.

4.3 Limits of the method

The positive results of the color correction, as seen in Fig. 6 suggest that the proposed model for the light transport and the underlying assumptions are valid. After the color correction, the blue image channel shows only a pure shadowgraphy image without any specular reflection of the lateral light sources. This result demonstrates that the presented method is able to produce standard shadowgraphy images in a high quality with the addition of further illumination angles of the droplet's interface that encode additional three-dimensional information of the droplets gas–liquid interface in the glare points as shown in Sect. 4.2.

The two evaluated methods (ASC and ISC) allow for an accurate reconstruction of the glare point and shadowgraph images by the correction of the mutual disturbance in the image channels, that resulted from polychromatic light and spectral sensitivity of the camera sensor. The analytical reconstruction (ASC) can reach a potentially higher reconstruction quality, if the spectral characteristics of all optical components can be determined accurately a-priori. If

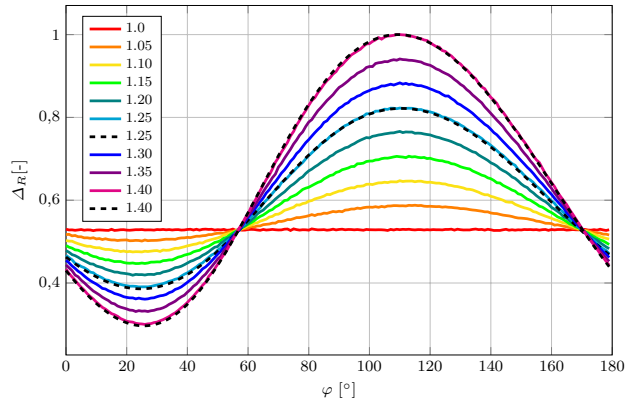

(a) Red glare point position

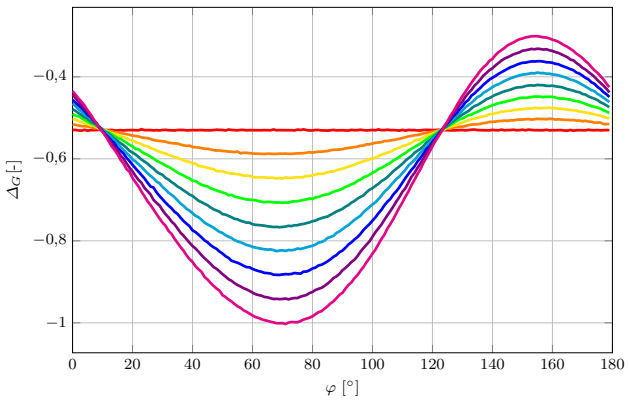

(b) Green glare point position

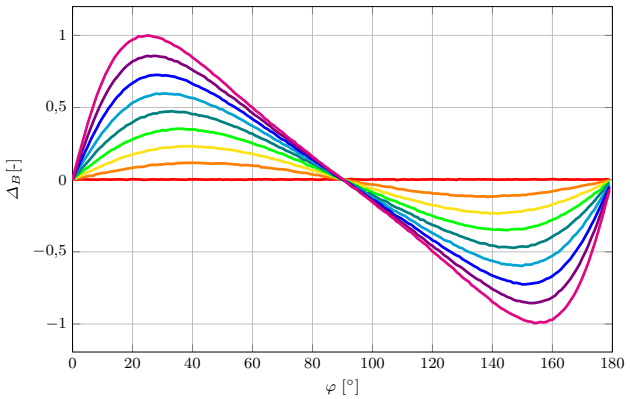

(c) Blue glare point position

Fig. 15 Positions of **a** the red and **b** green $p = 0$ glare points and **c** the blue $p = 1$ glare point relative to the shadowgraph contour of the droplet for increasing aspect ratios and normalized with the maximum absolute value. The dotted lines in **a** represent the analytical solution for comparison

such information is missing or incomplete, then the in-situ method (ISC) can be used to obtain the correction matrix, which introduces additional measurement imperfections, such as e.g., image noise.

It should be noted that the proposed color-correction models neglect chromatic aberration and dispersion. Due to the dependence of the refractive index on the wavelength of the incident light the (polychromatic) transmitted light would be deflected at a slightly different angle. Therefore, all glare points of order $p = 1$ and higher are affected by dispersion. Due to a higher amount of interactions with the gas–liquid interface the dispersion becomes increasingly severe for higher order glare points. As seen in Fig. 10 first, second and third order glare points, each with an increasing magnitude of dispersion can be observed in the experiments. Higher order glare points might appear in the images as well, however, since these lie close to the edges of the projected droplet, their spatial extent is very small compared to the lower order glare points so that the effects of dispersion can be neglected. A significant level of dispersion could lead to a faulty color correction, since different areas of the glare points on the images would be composed by different wavelengths. This effect would consequently distort the pixel-wise reconstruction.

For the optimal angular position of the lateral lights determined in Sect. 4.1 only $p = 0$ glare points do appear, which are produced by pure interface reflection and thus remain unaffected by dispersion. In contrast, the $p = 1$ glare point of the backlight is affected by dispersion, since it is refracted by the gas–liquid while entering and again while leaving the droplet. However, the influence of dispersion can be assumed to be negligibly small due to a small change in the index of refraction for the narrow-banded spectrum of the lateral LED light sources. The maximum angular dispersion in the first order glare point, i.e.. the deviation in the angles of the refracted light, can be estimated to be lower than 0.25° for the given spectra of the light sources using Snell's law (Hecht 2017).

Chromatic aberration causes differences in defocus and magnification between the color channels of the image, which can introduce errors to the color correction. Therefore, in the presented experiments a *Schneider-Kreuznach Apo-Componon 4.0/60* enlarging lens with apochromatic correction has been used to mitigate chromatic aberration. Even though beyond the scope of the present work, further investigation into the effect of chromatic aberration on the quality of the color correction is envisioned to further improve the accuracy of the method.

The intensity of the light sources was found to have no significant influence on the results of the color correction. The intensity of the color-corrected images scaled linearly with the light source intensity, but otherwise the channels had undergone the same color correction for different input intensities, thus validating the assumption of the linearity of the camera sensor. While the assumption of a linear response of the chip to the incident light holds true for intensities within the dynamic range, it neglects clipping in the regions of glare points and other highlighted image regions. Since one or potentially multiple color channels

can be clipped, changes in hue occur (Novak et al. 1990) and a proper calculation of the color correction is inhibited. The resulting loss of information for intensities above the dynamic range skews the correction function such that the mutual disturbance of the color channels cannot be fully removed in the overexposed frames, which has been discussed along selected frames in Fig. 6. Note that such frames can still be improved by the correction function. However, reduced light intensity mitigates this problem at the cost of likewise less pronounced glare points, especially on frames with larger areas of reflection. Therefore, the light source intensity needs to be fine tuned for conserving a maximum of information in dim and bright images.

The influence of the chosen elevation angle Φ on the resulting continuous registration and homogeneous intensity of recorded glare points has been already discussed in Sect. 4.1 for convex gas–liquid interfaces. Non-convex droplet shapes, which occur during the dynamic deformation of the droplet during impact, comprise multiple glare points at each position on the droplet surface that has the orientation Φ_c and θ_S. These glare points split and merge depending on the deformation of the gas–liquid interface as indicated e.g., in Fig. 4, where multiple glare points are visible at each capillary wave (see also Fig. 20 for the full time series). The appearance of $p = 0$ glare points on non-convex deformed droplets facilitates the encoding of additional three-dimensional information on a larger amount of points on the surface. However, a reconstruction of these droplet shapes will be more complicated in comparison with the spheroidal cap shape, for which an unambiguous encoding of the volumetric shape was confirmed in Sect. 4.2.

The overall good agreement of the glare-point positions in the experiment in dependence of the azimuthal angle θ to the theoretically expected positions (see Fig. 8) for all tested azimuthal angles, confirms the assumption of a circular cross section for the undeformed droplet. However, small differences in the position of the glare points were observed that might originate either from a deviation from the spherical shape and/or from alignment errors in the experimental setup. On the one hand, small changes in the scattering angle due to alignment errors in the azimuth angle of the lateral light sources, can result in significant changes of both glare-point intensity and position, which particularly cumulates for higher order glare points due to a larger number of interactions with the gas–liquid interface. In particular, the intensity increases sharply if the azimuth angle approaches the rainbow angle of the respective order of scattering, as can be seen in Fig. 18. The reduction of the measurement system to $p = 0$ and $p = 1$ glare points, therefore, significantly limits this error. On the other hand, alignment errors in the elevation angle of the lateral light sources result in a shift of the glare-point position. For low elevation angles the resulting error becomes negligible for small angular deviations, as the horizontal movement of the glare points is small due its trigonometrical relation to the elevation angle. For large elevation angles, however, this error source has to be considered.

A third error source are deformations of the droplet from the spherical shape, resulting in an elliptical cross section in the scattering plane for the lateral light sources. As shown in Sect. 4.2 the aspect ratio of an ellipsoidal droplet has a significant influence on the position of the glare points such that the deformation of the droplet in any axis has to be considered. Irregular deformations of the droplet will inevitably introduce deviations in the position of the glare point, which can lead to reconstruction errors. The present experiments of a droplet impinging in the normal direction onto a flat substrate, however, revealed no significant irregular deformations. Instead a deformation in the vertical direction from the detachment of the droplet at the needle was observed that causes a vertical oscillation and results in a spheroidal shape of the droplet. Note that the aspherical shape of the droplet in this case can be determined analogously to Sect. 4.2 from the position of the glare points.

5 Conclusions

The present work has elaborated on how an extension of the shadowgraphy measurement method by lateral light sources with distinct spectra can be used to gather additional information about the three-dimensional shape of a gas–liquid interface for the considered example of a liquid droplet impacting onto a solid surface. From the spectral power distribution of the light sources and the spectral sensitivity of the camera, a color correction function is determined by spectral integration, which allows for a clear separation of the two reflection images from the lateral light sources and the shadowgraphy image from the backlight. Application of the proposed color-correction function successfully demonstrated that the narrow-banded polychromatic light from three differently colored LEDs can be used to gather three distinct representations of the gas–liquid interface of an impinging droplet.

The presented method of capturing the reflection images from the lateral light sources in each one channel and the shadowgraphy image in the third channel of an RGB image allows for the use of a simple single-camera setup. This facilitates an easier calibration and reduces the complexity of a volumetric reconstruction from the images in comparison with a multi-camera setup, since no spatial or temporal matching of the produced images is necessary, which otherwise would require an exact measurement of the relative positions between the light sources and the camera in respect to the droplet. Note, however, that three representations captured with the single-camera RGB-shadowgraphy

setup certainly contain less information of the droplet interface than three individual pictures from cameras at different angles.

It was shown that the measurement setup is still able to produce a clear shadowgraphy image that is not impaired by the additional light sources. The two additional channels can be consequently considered as a pure extension to a canonical setup. The additional perspectives from the glare points on the gas–liquid interface by the lateral light sources lay the ground for a volumetric reconstruction of the phase boundary. Since the geometrical properties of the experimental rig—in particular the relative positions of the camera and the light sources in respect to the droplet—are known, features of the droplet surface can be reconstructed by the images of the glare points using the theory of geometrical optics, (as shown by Healey and Binford 1988; Horbach and Dang 2010). It was accordingly demonstrated that the additional information encoded in the glare points can be used to determine the aspect ratio and rotation angle of an ellipsoidal droplet. Future studies might extend this approach to more complicated shapes that appear during drop impact, including non-convex shapes with multiple glare points. Additional glare points from further viewing angles could then be employed to determine the larger number of parameters necessary to describe such complex geometries.

Lately, vast progress is made in the development of deep learning approaches for the volumetric reconstruction from single RGB images (see Saito et al. 2019; Lin et al. 2018, for instance), in which neural networks learn to infer three-dimensional shapes from image features. Such approaches could be utilized for the volumetric reconstruction of the gas–liquid interface of a droplet during impact. However, grayscale shadowgraphy images do provide only a relatively low amount of features. As such, any additional information encoded in the images by glare points is assumed to facilitate and in turn improve the reconstruction effort with such neural networks.

A strong and continuous glare point signal in the images over the complete range of droplet shapes during impact is required for a reconstruction of the whole droplet dynamics. The present work revealed that the optimal elevation angle for a continuous signal depends on the wettability of the substrate and is therefore case dependent, whereas an azimuth angle of 96.5° and 96.3° for the red and green lateral light sources, respectively, proved to be optimal to produce unambiguous glare point images. At the resulting scattering angle only zeroth order glare points appear, which prevents ambiguities from the reflection on the substrate from higher order glare points that were previously refracted by the gas–liquid interface. In addition, the position of zeroth order glare points is less affected by alignment errors of the lateral light sources in the scattering angle, compared to higher order glare points that see a larger number of interactions with the gas–liquid interface and therefore amplify the error at every interaction with the gas–liquid interface. However, higher order glare points have the potential for a more precise measurement of the surface orientation, therefore becoming suitable for experiments in which the measurement of small deviations in the droplets surface is of interest.

For axisymmetric droplets, different elevation angles for the two lateral light sources could be exploited to produce a higher number of unique illumination orientations on the droplet, which could be used in order to detect sites of air entrainment. Additional glare points from further illumination angles could be envisioned to encode the position and orientation of the gas–liquid interface at a larger amount of points to gather additional information. However, caution needs to be taken to ensure that the resulting glare points can be clearly distinguished from each other in order to avoid ambiguities.

In order to investigate the capability of the proposed method for capturing the three-dimensional droplet impact dynamics during a non-axisymmetric drop impingement further experiments—including the impingement of droplets onto structured surfaces—have to be conducted. While the measurement setup was presented along the example of an impinging droplet, it can be expanded to other applications involving gas–liquid interfaces like the two-phase flow in fuel cells, for instance.

Appendix

A: Analytical glare-point derivation

In this section, the analytical derivation of the position of a zeroth order glare point on an ellipsoidal droplet that is arbitrarily rotated around its third primary half-axis is detailed.

Points on the ellipsoid can be parameterized as

$$\begin{aligned}\mathbf{p}(\alpha,\beta) = \mathbf{f}_0 + \mathbf{f}_1 \cos\alpha\cos\beta \\ + \mathbf{f}_2 \cos\alpha\sin\beta + \mathbf{f}_3 \sin\alpha,\end{aligned} \tag{14}$$

where $\mathbf{f}_0$ denotes the ellipsoid's center point and $\mathbf{f}_{1,2,3}$ denote the ellipsoid's (orthogonal) primary half-axes, while $\alpha \in \left[-\frac{\pi}{2};\frac{\pi}{2}\right]$ and $\beta \in [0;2\pi[$ are the angular coordinates of the point. Furthermore, the normal vector at each point of the ellipsoid surface is known by

$$\begin{aligned}n(\alpha,\beta) = f_2 \times f_3 \cos\alpha\cos\beta + f_3 \times f_1 \cos\alpha\sin\beta \\ + f_1 \times f_2 \sin\alpha.\end{aligned} \tag{15}$$

The droplet's aspect ratio is consequentially defined as

$$A = \frac{\|f_1\|}{\|f_2\|}. \tag{16}$$

The camera recording the scene is modeled as a pinhole aperture and an image plane behind it. The droplet's center point f_0 and the known position of the pinhole aperture p_a form the optical axis. The image plane has a distance of d_{image} from p_a in direction of the optical axis and has the normal vector

$$n_{\text{image}} = \frac{p_a - f_0}{\|p_a - f_0\|}. \tag{17}$$

The parallel light of color c producing the glare point is emitted in known direction $d_{c,1}$. The direction of the light ray reflected from the droplet's surface to the pinhole aperture is denoted

$$d_{c,0} = \frac{p_a - p}{\|p_a - p\|}, \tag{18}$$

where p is the position of the glare point of color c on the droplet's surface.

A projection of the droplet in its rotational plane including all needed parameters is depicted in Fig. 16, where the third direction as well as the camera model are omitted for easier visualization.

The reflection condition—i.e., the angle of incidence equals the angle of reflection—can be written as

$$\begin{aligned} & d_{c,0} \cdot n = -d_{c,1} \cdot n \\ \Leftrightarrow \quad & n \cdot \left(d_{c,1} + d_{c,0}\right) = 0, \end{aligned} \tag{19}$$

since $d_{c,i}$ and the normal vector on the ellipsoid n (which corresponds to the point p) all have unit length.

Furthermore, the light direction vectors $d_{c,i}$ and the normal vector of the reflection plane must all lie in one plane, and therefore the conditions

$$d_{c,0} \cdot \left(d_{c,1} \times n\right) = 0 \tag{20}$$

must hold.

Solving the nonlinear system of equations formed by Eqs. 19 and 20 yields the angular coordinates α and β of the point p on the ellipsoid surface that reflects the light with the given initial direction into the aperture without crossing the ellipsoid. Since the ellipsoid is a convex body, the solution is unique.

Subsequently, the intersection between the linear equation

$$x = p_a + k d_{c,0} \tag{21}$$

and the image plane given by

$$n_{\text{image}} \cdot \left(p_{\text{image}} - x\right) = 0, \tag{22}$$

where p_{image} is an arbitrary point on the image plane, yields the position $p_{s,c}$ of the glare-point imprint on the camera sensor.

For a given aspect ratio A and droplet rotation φ, this set of equations can be numerically solved to reproduce the results from the renderings shown in Fig. 15. The analytical results using the full set of parameters, as also used in the rendering setup, are shown in Fig. 17 for the red glare point.

When the pixel positions of the glare points on the sensor Δ_R and Δ_G are known, the system can be solved numerically for the aspect ratio A and the rotation angle φ, yielding information about the droplet shape for a known optical setup. Since the position of a single glare point is enough to close the nonlinear system of equations, the

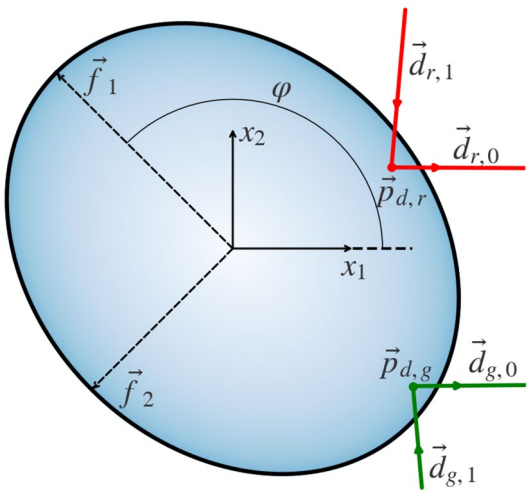

Fig. 16 Droplet projected in its rotation plane with red and green light beam, primary axes f_1 and f_2 and rotation angle φ

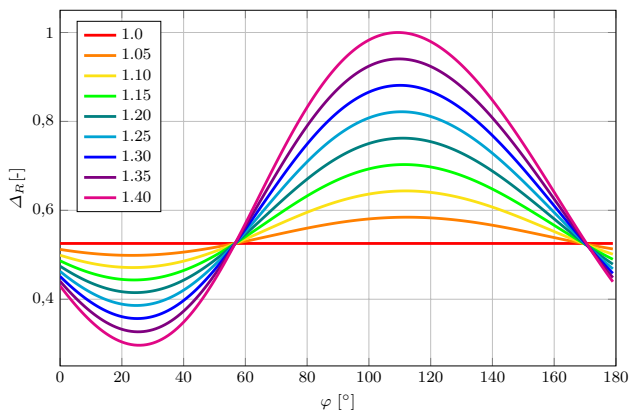

Fig. 17 Red glare-point positions calculated using the set of equations derived above

addition of a second glare point allows for an estimate of measurement errors and consequentially presents a measure for the validity of the chosen assumptions.

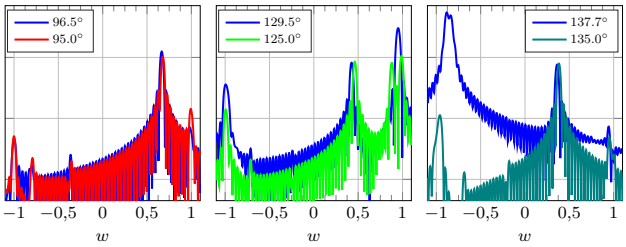

Fig. 18 Comparison of the glare-point images at scattering angles of **a** 95.0° and the ideal angle for $p = 0$ glare points 96.5°, **b** 125.0° and the $p = 3$ rainbow angle 129.5° and **c** 135.0° and the $p = 2$ rainbow angle 137.7° calculated by means of Eq. 4. The logarithmic glare-point intensity is plotted on the ordinate against the dimensionless variable w on the abscissa

B: Comparison of glare-point images at special scattering angles

C: Time series of RGB images

Comparison of the full series of RGB-frames shortly before

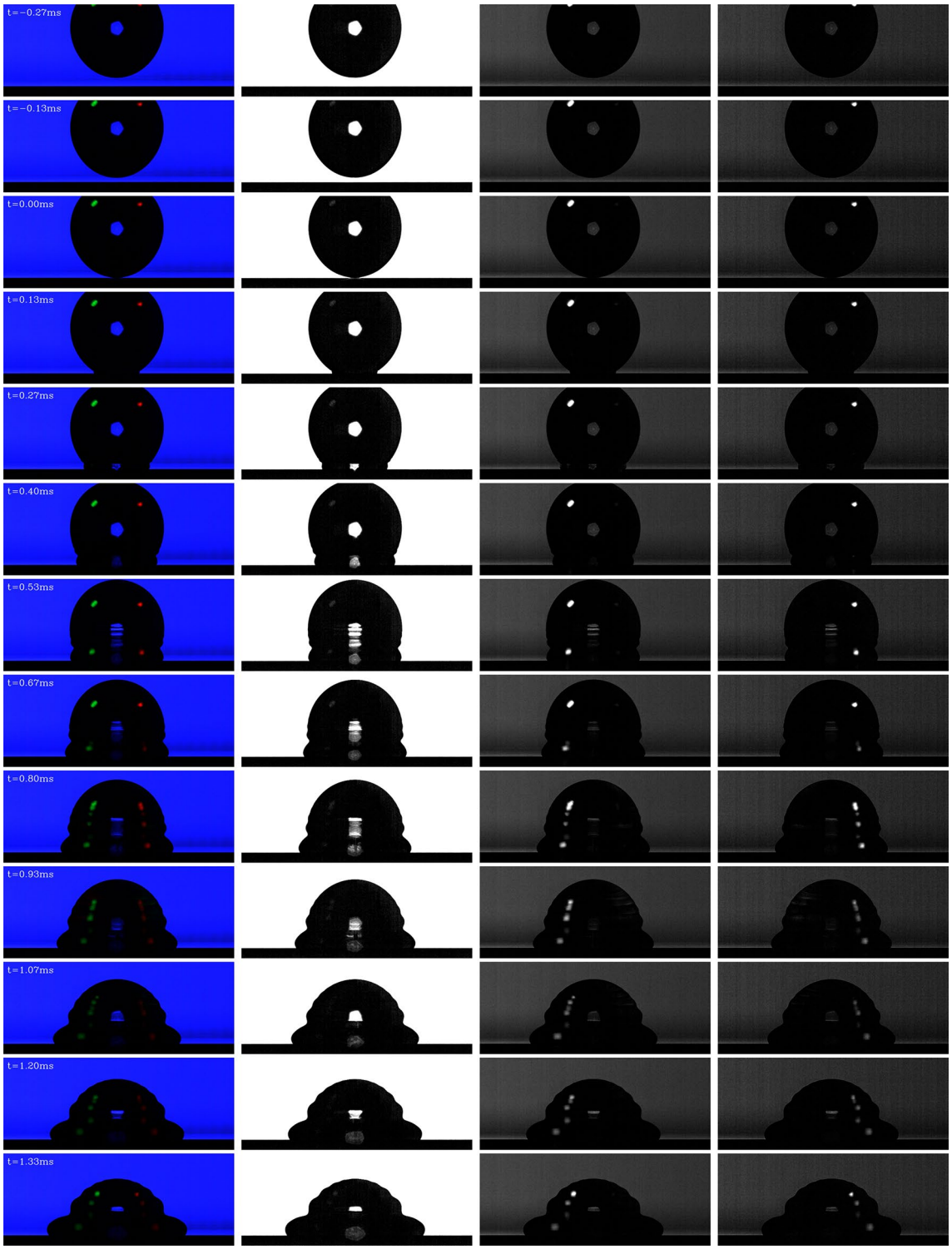

Fig. 19 Time series of an impinging water droplet onto a substrate with SiOx-coating; **a** RGB snap shots, captured with a *Photron Fastcam Nova R2* at 7,500 fps; separated **b** blue, **c** green and **d** red raw channels of **a**

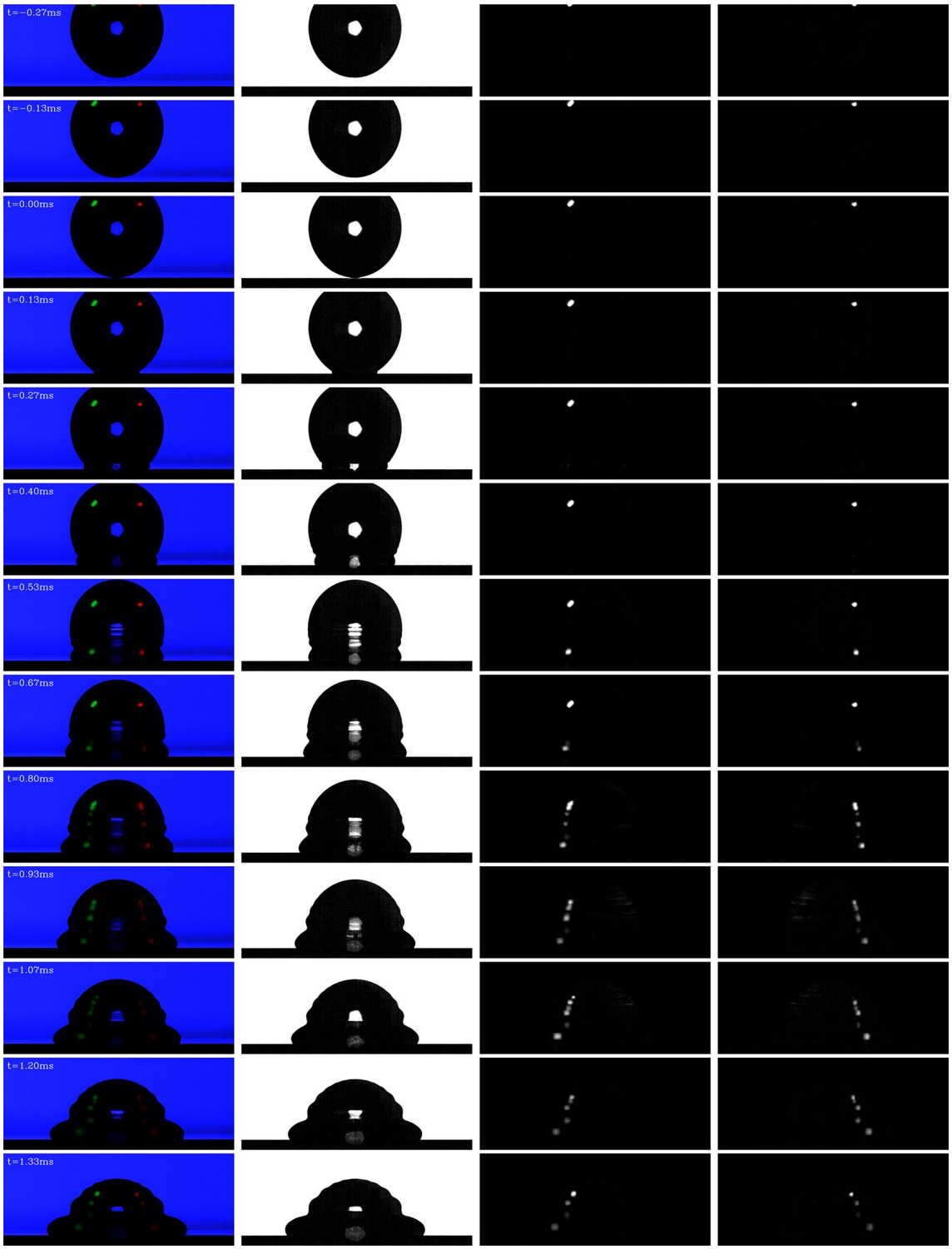

Fig. 20 Time series of an impinging water droplet onto a substrate with SiOx-coating; **a** RGB snap shots, captured with a *Photron Fastcam Nova R2* at 7,500 fps; separated **b** blue, **c** green and **d** red color-corrected channels of **a**

and after the drop impact between the raw images (Fig. 19) and the color-corrected images that result from the processing of the raw images with the ISC function (Fig. 20).

Author Contributions M. Dreisbach (Conceptualization, Design of experiments, Data acquisition, Data evaluation, Writing - original draft, Visualization), S. Blessing (Data acquisition, Design of experiments, Data evaluation, Writing - original draft, Visualization), F. Michaux (Design of experiments, review & editing), A. Brunn (Conceptualization, review & editing), A. Stroh (Conceptualization, review & editing), J. Kriegseis (Project administration, Design of experiments, Writing - review & editing)

Funding Open Access funding enabled and organized by Projekt DEAL.

Availability of data and materials The data that support the findings of this study are available upon request from the corresponding author.

Declarations

Ethical approval Not applicable.

Conflict of interest The authors declare that they have no conflict of interest.

References

Ashgriz N (2011) Handbook of atomization and sprays: theory and applications. Springer, Heidelberg

Blender Online Community (2018) Blender—a 3D modelling and rendering package. Blender Foundation, Stichting Blender Foundation

Born M, Wolf E, Bhatia AB, Clemmow PC, Gabor D, Stokes AR, Taylor AM, Wayman PA, Wilcock WL (1999) Principles of optics: electromagnetic theory of propagation, interference and diffraction of light, 7th ed. Cambridge University Press

Brunel M, Delestre B, Talbi M, Fromager M (2021) Interferometric imaging for the tomography of rough particles in a flow: a case study. Opt Commun 479(126):412

Bucciarelli D, Wendsche S, Klemm M, Sandbacka P, Ehoumanand C, Castagnini A, Quade G, Ghotbi O (2018) LuxCoreRender Project. LuxCoreRender Project

Cox R (1986) The dynamics of the spreading of liquids on a solid surface. Part 1. Viscous flow. J Fluid Mech 168:169–194

Dalili A, Chandra S, Mostaghimi J, Fan HC, Simmer JC (2016) Bubble entrapment and escape from sprayed paint films. Progress Organic Coatings 97:153–165

Debye P (1908) Das elektromagnetische feld um einen zylinder und die theorie des regenbogens. Phys Z 9(1464):775–778

Dehaeck S, Tsoumpas Y, Colinet P (2005) Extended glare point velocimetry and sizing for bubbly flows. Exp Fluids 39(2):407–419

Dehaeck S, Tsoumpas Y, Colinet P (2013) Analyzing droplets through digital holography and a 1d wavelet transform technique. In: Digital holography and three-dimensional imaging, OSA, Washington, DC, p DW3A.5

Dehaeck S, Tsoumpas Y, Colinet P (2015) Analyzing closed-fringe images using two-dimensional fan wavelets. Appl Opt 54(10):2939–2952

Fink V, Cai X, Stroh A, Bernard R, Kriegseis J, Frohnapfel B, Marschall H, Wörner M (2018) Drop bouncing by micro-grooves. Int J Heat Fluid Flow 70:271–278

Fu Y, Liu Y (2018) 3D bubble reconstruction using multiple cameras and space carving method. Measur Sci Technol 29(7):075206

Glover AR, Skippon SM, Boyle RD (1995) Interferometric laser imaging for droplet sizing: a method for droplet-size measurement in sparse spray systems. Appl Opt 34(36):8409–8421

Hale GM, Querry MR (1973) Optical constants of water in the 200-nm to 200-microm wavelength region. Appl Opt 12(3):555–563

Healey G, Binford TO (1988) Local shape from specularity. Comput Vis Gr Image Process 42(1):62–86

Hecht E (2017) Optics. Pearson, Harlow

Honkanen M (2009) Reconstruction of a three-dimensional bubble surface from high-speed orthogonal imaging of dilute bubbly flow. In: Mammoli AA, Brebbia CA (eds) Computational methods in multiphase flow V, WIT Press Southampton, UK, WIT Transactions on Engineering Sciences, pp 469–480

Horbach JW, Dang T (2010) 3D reconstruction of specular surfaces using a calibrated projector-camera setup. Mach Vis Appl 21(3):331–340

Horn B (1970) Shape from shading: a method for obtaining the shape of a smooth opaque object from one view. Tech. rep

Hovenac EA (1991) Calculation of far-field scattering from nonspherical particles using a geometrical optics approach. Appl Opt 30(33):4739–4746

Hu H, Wang B, Zhang K, Lohry W, Zhang S (2015) Quantification of transient behavior of wind-driven surface droplet/rivulet flows using a digital fringe projection technique. J Visual 18(4):705–718

van de Hulst HC (1981) Light scattering by small particles, unabridged and corrected republication of the work originally published in 1957 by John Wiley & sons, inc., n.y edn. Dover books on physics, LSC Communications and Dover Publications, Inc, New York

van de Hulst HC, Wang RT (1991) Glare points. Appl Opt 30(33):4755–4763

Ihrke I, Goidluecke B, Magnor M (2005) Reconstructing the geometry of flowing water. In: 10th IEEE international conference on computer vision (ICCV'05) Volume 1. IEEE, pp 1055–1060

Josserand C, Thoroddsen ST (2016) Drop impact on a solid surface. Annu Rev Fluid Mech 48(1):365–391

Kerker M (1969) The scattering of light and other electromagnetic radiation. Elsevier

Kinsey JL (1977) Laser-induced fluorescence. Ann Rev Phys Chem 28(1):349–372

Kistler S (1993) Hydrodynamics of wetting. In: Berg J (ed) Wettability. Marcel Dekker, New York, pp 311–430

Klinker G, Shafer SA, Kanade T (1988) The measurement of highlights in color images. Int J Comput Vis 2:7–32

König G, Anders K, Frohn A (1986) A new light-scattering technique to measure the diameter of periodically generated moving droplets. J Aerosol Sci 17(2):157–167

Laurentini A (1994) The visual hull concept for silhouette-based image understanding. IEEE Trans Pattern Anal Mach Intell 16(2):150–162

Lee HC, Breneman E, Schulte C (1990) Modeling light reflection for computer color vision. IEEE Trans Pattern Anal Mach Intell 12(4):402–409

Li C, Pickup D, Saunders T, Cosker D, Marshall D, Hall P, Willis P (2013) Water surface modeling from a single viewpoint video. IEEE Trans Visual Comput Graphics 19(7):1242–1251

Lin CH, Kong C, Lucey S (2018) Learning efficient point cloud generation for dense 3D object reconstruction. In: AAAI Conference on Artificial Intelligence (AAAI)

Masuk AUM, Salibindla A, Ni R (2019) A robust virtual-camera 3D shape reconstruction of deforming bubbles/droplets with additional physical constraints. Int J Multiph Flow 120(103):088

Mie G (1908) Beiträge zur optik trüber medien, speziell kolloidaler metallösungen. Ann Phys 330(3):377–445

Morris NJW, Kutulakos KN (2011) Dynamic refraction stereo. IEEE Trans Pattern Anal Mach Intell 33(8):1518–1531

Nitsche W, Brunn A (2006) Strömungsmesstechnik. Springer, Heidelberg

Novak CL, Shafer SA, Willson RG (1990) Obtaining accurate color images for machine-vision research. In: Brill MH (ed) Perceiving, Measuring, and Using Color. International Society for Optics and Photonics, SPIE, vol 1250, pp 54 – 68

Nussenzveig HM (1977) The theory of the rainbow. Sci Am 236(4):116–127

Qian Y, Gong M, Yang YH (2017) Stereo-based 3D reconstruction of dynamic fluid surfaces by global optimization. In: 2017 IEEE Conference on Computer Vision and Pattern Recognition (CVPR), IEEE, pp 6650–6659

Rioboo R, Tropea C, Marengo M (2001) Outcomes from a drop impact on solid surfaces. Atomiz Sprays 11(2):155–166

Rioboo R, Marengo M, Tropea C (2002) Time evolution of liquid drop impact onto solid, dry surfaces. Exp Fluids 33:112–124

Ríos-López I, Karamaoynas P, Zabulis X, Kostoglou M, Karapantsios TD (2018) Image analysis of axisymmetric droplets in wetting experiments: a new tool for the study of 3D droplet geometry and droplet shape reconstruction. Colloids Surf A 553:660–671

Roth A, Kristensson E, Berrocal E (2020) Snapshot 3D reconstruction of liquid surfaces. Opt Express 28(12):17906–17922

Saito S, Huang Z, Natsume R, Morishima S, Kanazawa A, Li H (2019) PIFu: pixel-aligned implicit function for high-resolution clothed human digitization. In: Proceedings of the IEEE/CVF international conference on computer vision (ICCV)

Settles GS (2001) Schlieren and shadowgraph techniques. Springer, Berlin

Shafer SA (1982) Describing light mixtures through linear algebra. J Opt Soc Am 72(2):299–300

Shafer SA (1984) Optical phenomena in computer vision. Technical Report TR135, Carnegie-Mellon University, Computer Science Department, Pittsburgh, PA

Swinehart DF (1962) The beer-lambert law. J Chem Educ 39(7):333

Takeda M, Ina H, Kobayashi S (1982) Fourier-transform method of fringe-pattern analysis for computer-based topography and interferometry. J Opt Soc Am 72(1):156

Wakeham WA, Assael MJ, Marmur A, Coninck JD, Blake TD, Theron SA, Zussman E (2007) Material properties: measurement and data; contact angle. In: Tropea C, Yarin AL, Foss JF (eds) Springer handbook of experimental fluid mechanics. Springer, Heidelberg, pp 106–118

Walker JD (1976) Multiple rainbows from single drops of water and other liquids. Am J Phys 44(5):421–433

Wang F, Theuwissen A (2017) Linearity analysis of a CMOS image sensor. Electron Imaging 29(11):84–90

Wörner M, Samkhaniani N, Cai X, Wu Y, Majumdar A, Marschall H, Frohnapfel B, Deutschmann O (2021) Spreading and rebound dynamics of sub-millimetre urea-water-solution droplets impinging on substrates of varying wettability. Appl Math Model 95:53–73

Yarin A (2005) Drop impact dynamics: splashing, spreading, receding, bouncingá. Annu Rev Fluid Mech 38:159–192

Yarin AL, Roisman IV, Tropea C (2017) Collision Phenomena in Liquids and Solids. Cambridge University Press, Cambridge

Yu M, Quan H (2013) Fluid surface reconstruction based on specular reflection model. Comput Anim Virt Worlds 24(5):497–510

Zhang K, Wei T, Hu H (2015) An experimental investigation on the surface water transport process over an airfoil by using a digital image projection technique. Exp Fluids 56(9):1